PHYSICAL INSIGHT INTO SCRAMJET INLET BEHAVIOUR VIA MULTI-OBJECTIVE DESIGN OPTIMISATION

H. Ogawa and R. R. Boyce
Centre for Hypersonics, School of Mechanical and Mining Engineering,
The University of Queensland

Keywords: *Scramjet inlet, Hypersonic aerodynamics, Multi-objective design optimisation*

Abstract

Scramjet propulsion is a promising technology for reliable and economical access to space and high-speed atmospheric transport. The inlet plays a key role in determining the performance of scramjets, in particular for the axisymmetric class of scramjet engines that are currently explored due to their advantages in numerous aspects. In the present study a multi-objective design optimisation (MDO) has been conducted with respect to four major inlet design criteria: compression efficiency, drag, adverse pressure gradient, and exit temperature. The former three criteria are used as the objective functions and the last as the constraint function to evaluate the inlet flowfields in the state-of-the-art coupled CFD / MDO approach. The influential parameters and key physics have been identified by scrutinising the flowfields that have been obtained as an outcome of the optimisation.

1 Introduction

Hypersonic airbreathing propulsion offers the potential for reliable and economical transport for access to space and high-speed atmospheric cruise. In particular, scramjets (Supersonic Combustion Ramjets) are a promising technology that can enable efficient and flexible transport systems, having marked milestones in the last decade: world's first supersonic combustion in HyShot II Program in July 2002 [1, 2], the fastest atmospheric flights recorded by NASA's X-43A

Nomenclature

x [m]	:	streamwise coordinate
r [m]	:	radial coordinate *or* radius
s [m]	:	coordinate along inlet surface
l_i [m]	:	ramp length of ith ramp
θ_i [deg]	:	ramp angle of ith ramp
$\Delta\theta_i$ [deg]	:	ramp angle increment of ith ramp
M	:	Mach number
p [Pa]	:	static pressure
dp/ds [Pa/m]	:	surface pressure gradient
T [K]	:	static temperature
$\bar{T}$	:	stream-thrust-ave. temperature
η_B	:	compression efficiency
h [J/kg]	:	enthalpy
s [J/kg·K]	:	entropy
S	:	first-order sensitivity index
S_T	:	total sensitivity index
O	:	point on Pareto optimal front
F	:	point among feasible individuals

Subscripts

∞	:	freestream value
max	:	maximum value
rel	:	relative value
1	:	value at inlet entrance
2	:	value at inlet exit
c	:	property of combustor
t	:	property of leading-edge tip

scramjet-powered vehicles in the Hyper-X program at Mach 6.8 (March 2004) and 9.6 (November 2004) [3], and the most recent flight by Boeing X-51A WaveRider, which recorded the longest scramjet burn duration at Mach 5 in May 2010 [4].

Fig. 1 Axisymmetric scramjet (upstream view) [5]

An axisymmetric scramjet configuration (Fig. 1) is currently being explored, following the performance demonstrated in shock tunnel testing [5]. Scramjet engines typically operate in a sequential process (Fig. 2): hypersonic inflow is captured and compressed through the inlet to the desired high pressure and temperature. Fuel is injected and mixed with air and combustion takes place in the downstream chamber. The reacted gas is expanded by the nozzle to produce thrust. Combined with innovative concepts including inlet fuel injection and radical-farming shock-induced combustion, the simple axisymmetric configuration can bring about numerous advantages over complex three-dimensional geometries in aerodynamic and combustion efficiency, aerothermal and structural management as well as manufacture [6, 7].

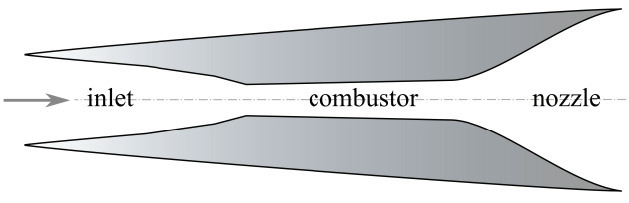

Fig. 2 Schematic of an axisymmetric scramjet

Axisymmetric scramjet inlets with high internal compression, however, are inherently difficult to start spontaneously during flight, highly susceptible to unstart. Numerical investigation has recently been conducted at The University of Queensland (UQ) in order to address this issue and probe the underlying physics. Time-accurate computations have revealed a substantial influence of shock wave / boundary layer interactions on the inlet starting mechanism, with formation of separation at compression corners playing an essential role in the unstarting process [8]. Various techniques have been examined numerically to overcome the problem, where instantaneous diaphragm rupture (with bleed addition) and sliding doors (or diaphragm erosion) have been found to be particularly effective in starting the inlets [9]. Despite the remarkable effectiveness of these methods, it is of crucial importance to design inlets which are naturally less susceptible to undesirable unstarting events for reliable and stable inflight operation of axisymmetric scramjets.

Design criteria for high-performance scramjet inlets typically include: efficient compression with minimum viscous / shock losses, minimum contribution to the vehicle drag, and minimum adverse pressure gradient to suppress separation, while achieving adequate compression to induce ignition [10]. Such multi-objective design would represent a formidable challenge for conventional optimisation approaches due to highly complex aerodynamic phenomena and coupled effects that result from geometric specifications. An advanced multi-objective design optimisation (MDO) capability featuring evolutionary algorithms with surrogate modelling has been developed at the University of New South Wales campus at the Australian Defence Force Academy (UNSW@ADFA) [11, 12]. Coupling these MDO algorithms with state-of-the-art CFD codes has realised a sophisticated design methodology, which has recently been applied successfully to various scramjet optimisation problems [13, 14].

A triple-objective optimisation has been performed for axisymmetric scramjet inlets in the present research. The results and flowfields have been probed to identify key geometric parameters and the underlying flow physics.

2 Approaches

2.1 Configurations

2.1.1 Inlet geometry

The inlet to be optimised in this paper comprises three ramps, as schematically shown in Fig. 3. The internal geometry is represented by eight parameters: the leading-edge nose-tip radius r_t, ramp lengths $l_{1,2,3}$, first ramp angle θ_1, ramp angle increments $\Delta\theta_{2,3}$, and exit radius r_c (or combustor radius). The inlet radius is fixed at 0.075m to ensure constant mass flow entry, which effectively makes one of the ramp parameters dependent on the others for a given value of the combustor radius r_c (l_1 is chosen as such a dependent variable in this study). Also fixed is the leading-edge nose-tip radius r_t=0.5mm in order to focus on the influence of ramp geometries by freezing the entropy layer effect originating from the leading edge. These assumptions, in effect, leave six parameters (l_2, l_3, θ_1, $\Delta\theta_2$, $\Delta\theta_3$ and r_c) as design variables, or decision variables for optimisation.

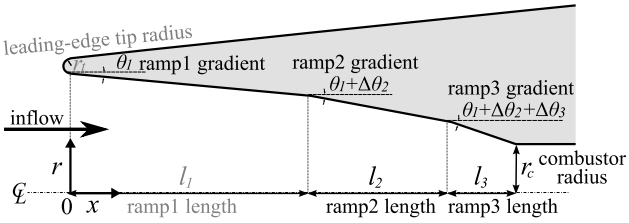

Fig. 3 Inlet design parameters

2.1.2 Flow conditions

The freestream conditions are $M_\infty = 8.0$, $p_\infty =$ 1197Pa, and $T_\infty = 226.5$K, assuming scramjet operation on a constant dynamic pressure trajectory of 53.6kPa at an altitude of 30km. The rate of the mass flow captured by the constant inlet area is 0.78kg/s. The Reynolds number based on the inlet radius (0.075m) is $Re_\infty = 2.26 \times 10^5$.

2.2 Computational Fluid Dynamics

2.2.1 Computational methods

Inlet flowfields are computed by utilising the state-of-the-art commercial solver CFD++ [19]. An implicit algorithm with second order spatial accuracy is used to solve the Navier-Stokes equations for steady flowfields and convergence is accelerated by the multigrid technique. Standard air in thermochemical equilibrium state is assumed for the gas and the inlet surface is assumed to be a cold wall at 300K. The inflow is assumed to be fully turbulent and modelled by the two-equation SST $k-\omega$ RANS model due to its demonstrated fidelity in the presence of adverse pressure gradient [20]. Computations are performed until the energy residual drops to the order of 10^{-5}, based on a convergence dependency study, where all objective functions have been found to vary less than 0.07% at higher orders.

2.2.2 Computational mesh

Two-dimensional structured meshes are generated by Glyph scripting within the commercial grid generator Pointwise [21] for the inlet geometry defined by the design parameters, as described in 2.1.1. The mesh comprises 21582 cells (219 nodes in the streamwise and 100 nodes in the wall-normal direction) with a non-dimensional distance value y^+ of 0.32 on average at the wall surface, as seen in Fig. 4 for the baseline geometry[1]. This mesh resolution has been selected, based on a mesh sensitivity study conducted for various resolutions such as coarse (219×100 nodes), nominal (432×200 nodes), fine (864×400 nodes) and superfine (1728×800 nodes) ones. It has been found that coarse meshes can result in up to 9% difference in the compression efficiency η_B, as compared to the superfine ones, while no essential difference has been observed in the flowfields. The coarse resolution has thus been selected in order to minimise the computational cost on the assumption that the major tendencies are maintained for the objective and constraint functions owing to the reasonable

[1] $\theta_1 = 5.0°$, $l_2 = 0.069$m, $\Delta\theta_2 = 5.3°$, $l_3 = 0.039$m, $\Delta\theta_3 = 3.3°$, $r_c = 0.035$m.

agreement in the flowfields involving shock wave / boundary layer interactions.

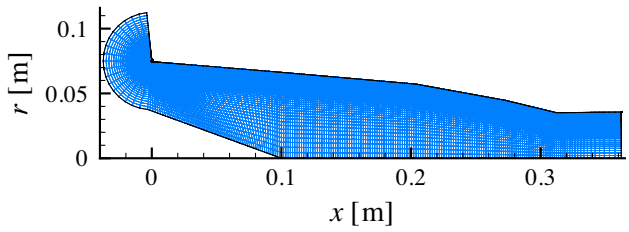

Fig. 4 Computational mesh for the baseline inlet geometry

2.3 Design Optimisation

2.3.1 Optimisation algorithms

The optimisation is performed in an iterative manner. Fig. 5 schematically shows the optimisation chain which consists of mesh generation (pre-processing), CFD computation (evaluation), post-processing and optimisation algorithms.

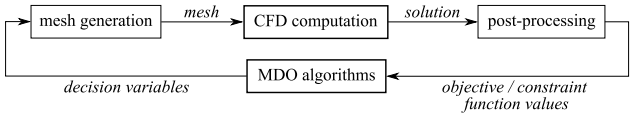

Fig. 5 Optimisation loop

Population-based evolutionary algorithms developed at UNSW@ADFA are employed as the MDO algorithms [11, 12]. In particular, use is made of the elitist non-dominated sorting genetic algorithm (NSGA-II)[22]. Optimisation occurs over generations with a population of 64 individuals. A simulated binary crossover and polynomial mutation are used as recombination operators at a given probability (1.0 and 0.1, respectively) with a specified distribution index (10 and 20, respectively). The optimisation process is efficiently assisted by various surrogate models including the response surface models, kriging approximations and radial basis functions. Among these models the one with the least error within a threshold of 10% is adopted to predict the objective and constraint functions in lieu of actual CFD evaluation and all individuals that are estimated to be superior to the present elitists are verified by true CFD evaluation. All members in the population pool are truly evaluated by CFD every 5 generations, when the surrogate models are trained by using 90% of the solutions from the archive, which stores all solutions that are evaluated by true evaluation. Variance-based global sensitivity analysis is performed to investigate the influence of decision variables on the objective functions, based on the surrogate model with the highest prediction accuracy as at the final generation. Evaluation is made for 10,000 sample data points represented by Sobol quasi-random numbers within the decision variable ranges [23, 24].

2.3.2 Optimisation problem

Three characteristic parameters are chosen and used as objective functions in order to achieve the optimisation goal to satisfy the inlet design criteria. The inlet performance is assessed by the compression efficiency $\eta_B \equiv \frac{h(p_2,s_1)-h_1}{h_2-h_1}$, which is able to account for both shock and viscous losses less sensitively to non-uniform exit flows and inlet heat transfer, as compared to other efficiency parameters [10, 15, 16]. The inlet drag is evaluated as the second objective function to be minimised. The third objective is to minimise the greatest local adverse pressure gradient on the surface, which if too large would be responsible for boundary layer separation and unstart. A constraint function, a measure of the solution feasibility, is imposed on the mean temperature at the inlet exit (combustor entrance); this must be greater than 850K, a typical self-ignition temperature [17], since little is known on what constitutes desirable flow profiles at the combustor entrance [16]. The compression efficiency and mean temperature are evaluated by using stream-thrust averaged values [18]. The optimisation problem can thus be stated as follows:

$$\begin{aligned} \text{minimise:} \quad & (1)\ 1-\eta_B \\ & (2)\ \text{Drag} \\ & (3)\ dp/ds_{\max} \\ \\ \text{subject to:} \quad & \bar{T_2} \geq 850\text{K} \end{aligned}$$

3 Results

3.1 Optimisation results

3.1.1 Pareto optimal front

The optimisation has been performed until little variation has been observed in the population. Fig. 6 shows all the individuals that have been evaluated by CFD up to the 50th generation[2]. The optimal individuals among the feasible solutions form a Pareto optimal front mainly with respect to the compression efficiency η_B and maximum adverse pressure gradient $dp/ds_{\max}$, while a discrete boundary between the feasible and infeasible solutions according to the exit temperature criterion is found to lie at an approximate drag value of 160N.

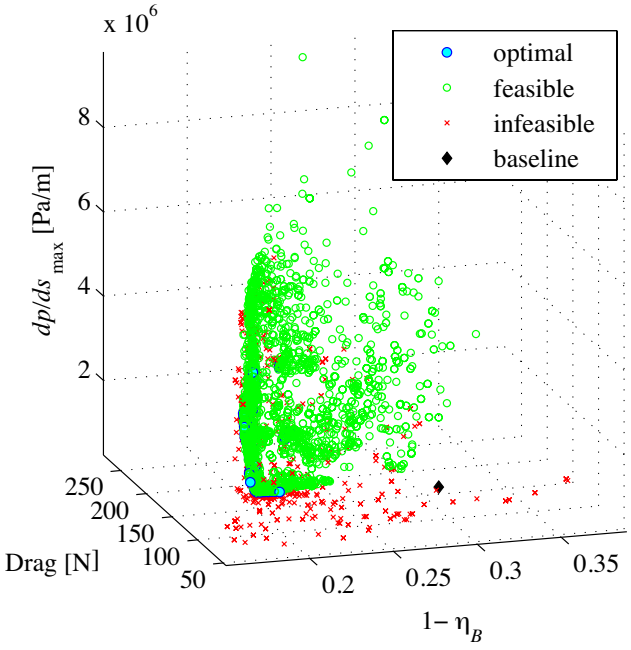

Fig. 6 Optimal population and individuals (3329 solutions in total) as at the 50th generation

In order to investigate the results from the optimisation, a few points have been selected that are different in one objective function but similar in the other two, thus allowing comparison. The values of such representative cases are shown in Table 1 and the points are displayed in Fig. 7 along with the 64 non-dominated individuals which constitute the Pareto optimal front.

[2]Note that the majority of the 64 optimal individuals are submerged by the other points in Fig. 6.

Table 1 Objective and constraint values of the representative points

	$1-\eta_B$	Drag [N]	$\frac{dp}{ds}_{\max}$ [Pa/m]	$\overline{T_2}$ [K]
O_1	0.203	158	8.95×10^5	850
F_1	0.298	167	1.27×10^6	879
F_2	0.305	249	1.48×10^6	1108
F_3	0.204	159	5.80×10^6	855
base	0.301	124	7.13×10^5	736

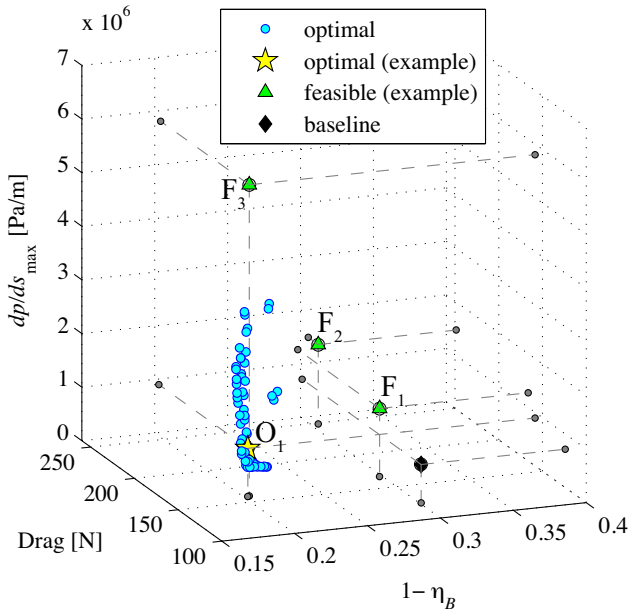

Fig. 7 Pareto optimal front and example points

3.1.2 Decision variables

Plotted in Fig. 8 are the objective functions and decision variables for the representative optimal and example individuals, along with the bounding values at the top and bottom of the bars. Considerable variations can be observed in the ramp angle θ_1 and increments $\Delta\theta_{2,3}$ as well as the exit radius r_c among the optimal and feasible solutions, whereas the levels of the ramp lengths $l_{2,3}$ are relatively similar.

3.1.3 Sensitivity analysis

Global sensitivity analysis has been performed, based on the prediction from the surrogate model

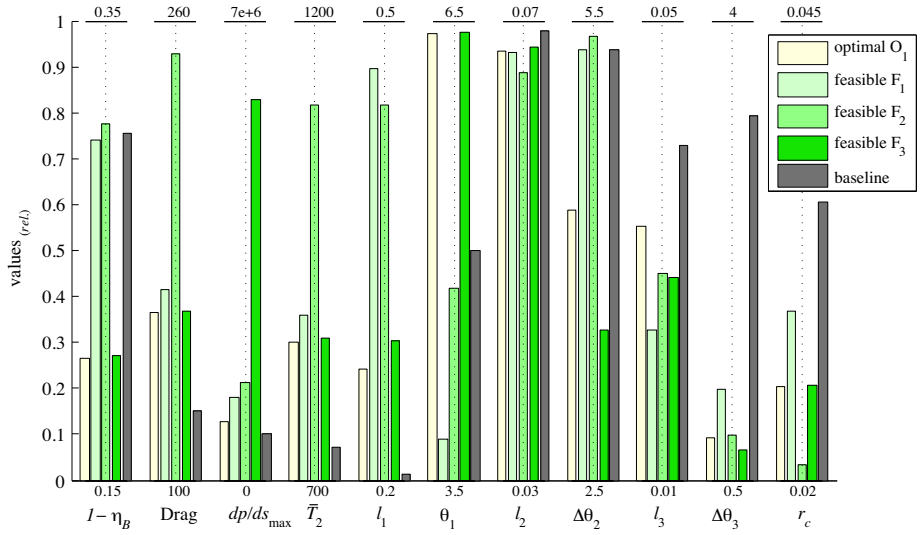

Fig. 8 Objective functions and decision variables for selected individuals

with the least error [23, 25]. The first-order sensitivity index S represents the main effect of the input parameter (decision variable) on the output parameter (objective / constraint function). The total sensitivity index S_{T} is the sum of all the effects including first-order as well as higher-order ones, which account for the interactions with the other parameters. The sensitivity indices S's and S_{T}'s are plotted in Fig. 9 for the compression efficiency η_B, whose indices are found to be very similar to those for the drag and exit temperature $\bar{T}_2$[3]. It can be seen that the radius at the inlet exit r_c exerts dominant influence on these objective and constraint functions, while the ramp lengths $l_{2,3}$ have negligible effects both in the first-order and total sensitivity indices.

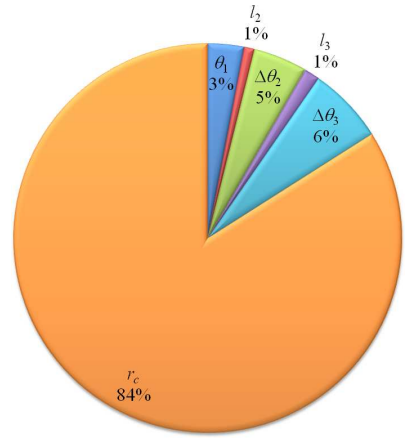

(a) first-order sensitivity index S

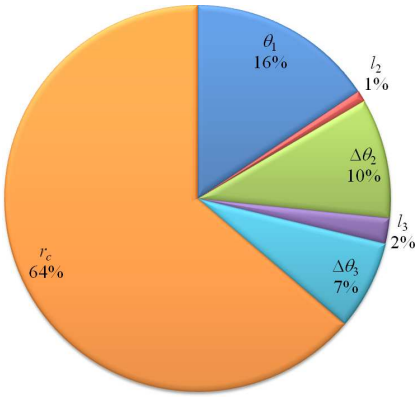

(b) total sensitivity index S_{T}

Fig. 9 Global sensitivity analysis on η_B

[3]No reasonable indices have been obtained for the maximum pressure gradient $dp/ds_{\max}$ due possibly to the highly local nature of the variable, as compared to the others, which are integral quantities.

3.2 Observations

3.2.1 *Compression efficiency*

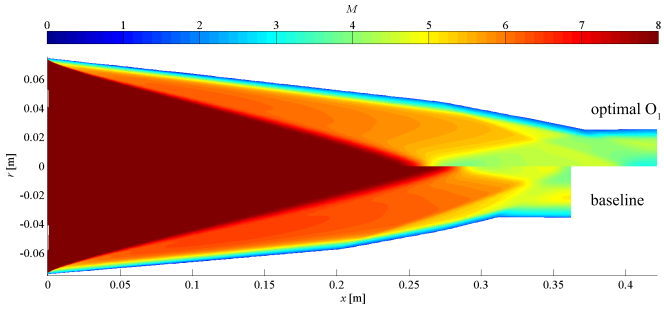

(a) Mach number

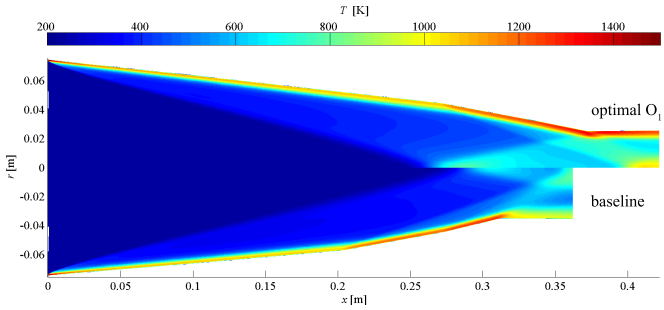

(b) temperature

Fig. 10 Flowfields of optimal O_1 and baseline geometries

The optimal individual O_1 and feasible solution F_3 are found in Fig. 7 to yield higher compression efficiency in comparison with $F_{1,2}$ and the baseline geometry. It indicates, by the definition of η_B, that O_1 and F_3 compress the inflow in an efficient manner that is closer to isentropic than $F_{1,2}$ and the baseline geometry, incurring less losses from shock waves and viscous effects. The flowfield of O_1 is compared with that of the baseline in Fig. 10. The flow profiles at the inlet exit (combustor entrance) are plotted and compared in Fig. 11 with respect to the Mach number and total pressure. It can be seen that similar levels of flow diffusion are achieved at the centre line ($M = 4.3 - 4.5$) for all geometries excepting F_1 (Fig. 11 (a)), while the centre-line total pressure varies considerably between the cases (Fig. 11 (b)). The largest compression is attained by F_2 with the largest total pressure loss whereas the mildest compression is achieved by the baseline with the smallest total pressure loss, but both geometries incur the same level of losses in the compression efficiency. It suggests the existence of a mechanism behind that enables particular geometries such as O_1 and F_3 to achieve efficient compression, which is a subject to be identified by further scrutinisation.

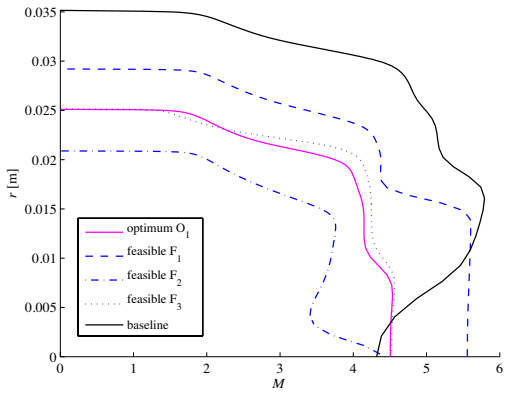

(a) Mach number

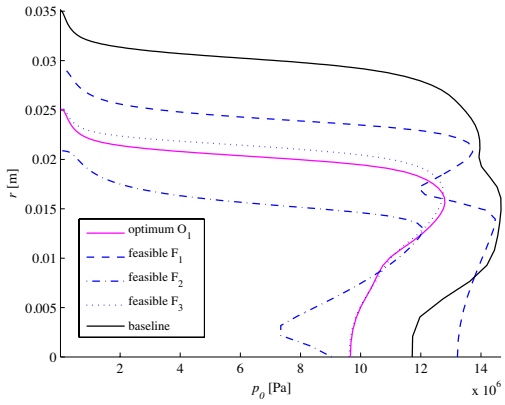

(b) total pressure

Fig. 11 Flow profiles at the inlet exit

3.2.2 *Drag*

The inlet drag is compared in Fig. 12, including the breakdown of the viscous and pressure (inviscid) contributions. The higher drag level incurred by O_1 compared to the baseline can be attributed

to a smaller exit radius r_c, i.e. an increased wall area on which the pressure can act in the x direction. A somewhat higher drag is incurred by F_1, where the viscous contribution is augmented by a larger skin friction drag on the extended inlet surface, as seen in Fig. 13. Nearly the same level of pressure drag, on the other hand, is incurred by O_1 and F_1 despite a larger frontal area of O_1, which is attributed to the higher pressure acting on a large extent of the second and third ramp due to the impingement of the main shock reflected on the symmetry axis in the case of F_1 (Fig. 13). The greatest drag is experienced by F_2 due to its smallest exit radius r_c, while the viscous drag is comparable to F_1 due to the similar inlet length (Fig. 14).

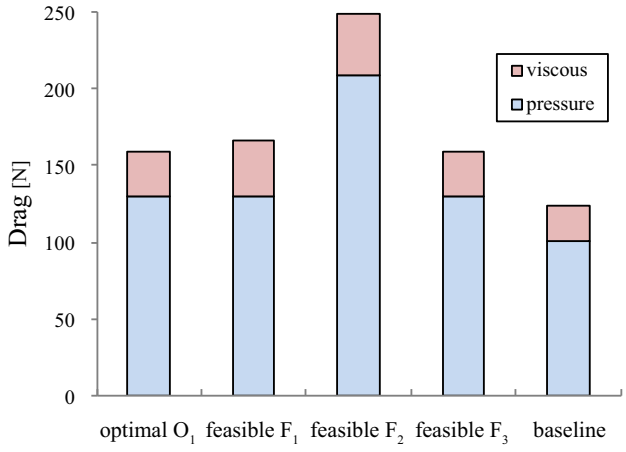

Fig. 12 Drag contribution and breakdown

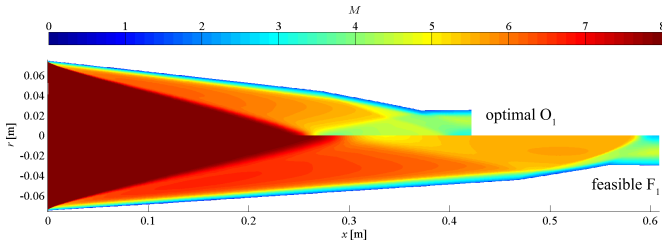

Fig. 13 Mach number distributions of optimal O_1 and F_1 geometries

3.2.3 Pressure gradient

Adverse pressure gradient is a primary factor that is responsible for incipient flow separation. It has been found in Fig. 7 that the feasible solution F_3 is subject to a substantially higher degree of adverse pressure gradient, compared to the optimal O_1 geometry, while the compression efficiency and drag levels are virtually the same for both. The flowfields are compared in Fig. 15, where both geometries indeed appear to be very similar. However, the wall pressure distributions plotted in in Fig. 16 show a perpendicular rise immediately upstream of the inlet end in the F_3 case, which has led to an acute adverse gradient. This can be attributed to a smaller increment of the second ramp $\Delta\theta_2$ of F_3. It renders the third ramp extend slightly further downstream, where the reflected shock wave impinges, subsequently causing a large pressure gradient, which was felt by F_3 but avoided by O_1.

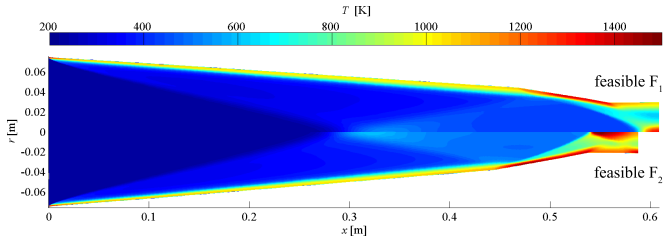

Fig. 14 Temperature distributions of F_1 and F_2 geometries

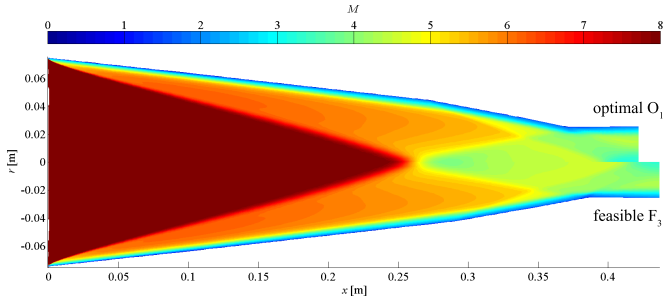

Fig. 15 Mach number distributions of optimal O_1 and F_3 geometries

3.2.4 Temperature at exit

The flow temperature at the inlet exit plays a key role in the ignition process in the combustion chamber, particularly for radical-farming shock-induced combustion, where a sufficient amount of heat release is required [6, 7]. The stream

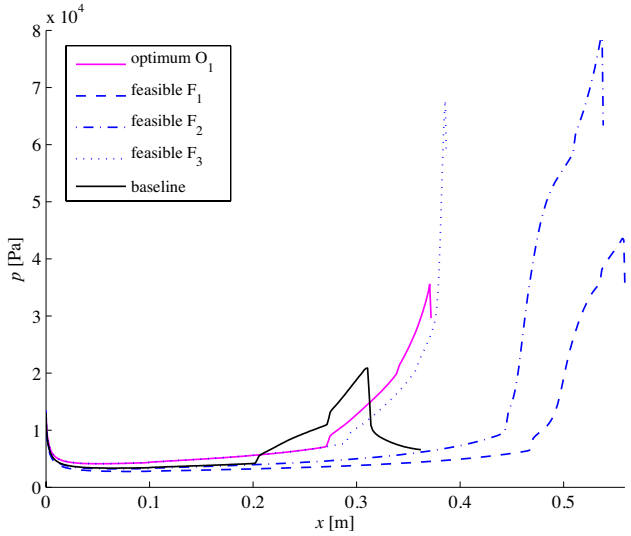

Fig. 16 Wall pressure distributions

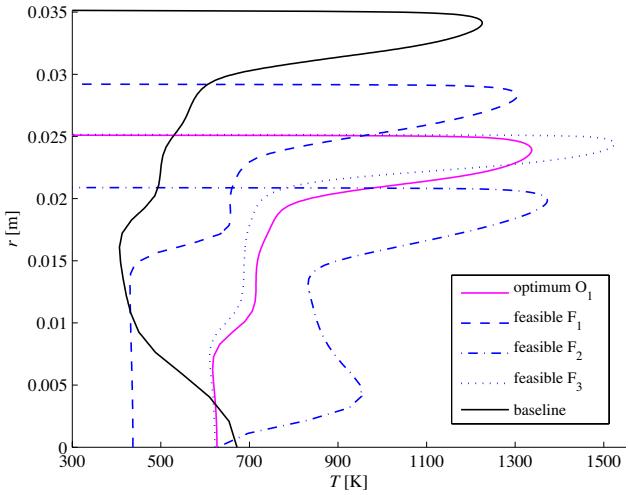

Fig. 17 Temperature profiles at inlet exit

thrust average of the outflow temperature is thus employed as a constraint function to judge the feasibility of the individuals. The temperature at the inlet exit is plotted and compared in Fig. 17, where the feasible solutions are found to have satisfied the temperature requirement for self ignition ($\bar{T}_2 \geq 850$K) in various ways; F_1 has achieved the minimum temperature with a relatively large exit radius r_c, whereas F_2 has attained a high temperature of $\bar{T}_2 = 1108$K, well over the self-ignition temperature, with a smaller radius close to the lower bound of the r_c range. The optimal O_1 and feasible F_3 solutions lie in the middle, the latter of which has a narrower and higher peak due to a slight modification of the shock structure caused by a smaller value of $\Delta\theta_2$.

It has been noted in the plot of the final population and individuals (Fig. 6) that the feasibility of the solutions distinctly changes across a certain level of drag, suggesting some correlation between the drag and exit temperature. The values for these two quantities are plotted in Fig. 18, which shows a remarkable, seemingly linear correlation between the drag and exit temperature. This is a subject for further investigation, but these two properties may well be closely linked by the exit radius, which predominantly dictates both the drag (as discussed in 3.2.2) and the temperature (as seen in Fig. 17).

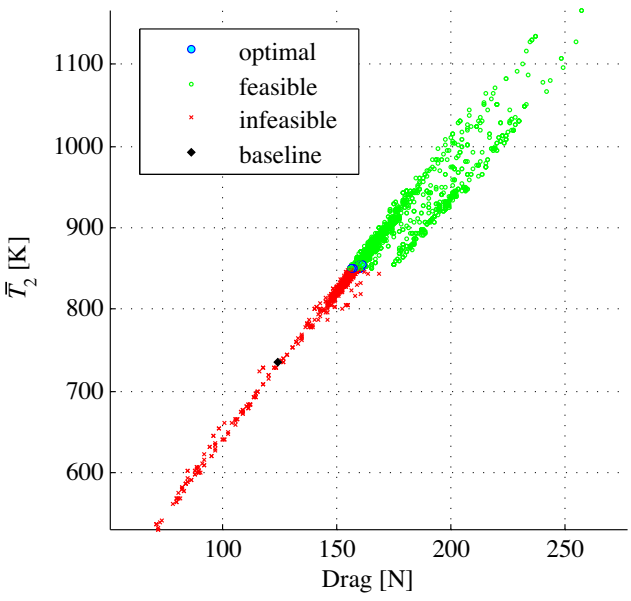

Fig. 18 Correlation between drag and exit temperature

4 Conclusions

A multi-objective design optimisation has been performed for axisymmetric scramjet inlets with respect to four design criteria, i.e. the compression efficiency, drag and maximum adverse pressure gradient as objective functions, and the exit temperature as a constraint function. The viscous equilibrium flowfields have been evaluated numerically by utilising a CFD solver and surrogate-assisted evolutionary algorithms have been applied to optimise the inlet geometry comprising three ramps. A Pareto optimal front has been reached as a result of optimisation and the flowfields have been scrutinised for the representative cases in order to gain insight into the underlying physics.

The combustor radius has been found to play a dominant role in most objective and constraint functions, while the ramp lengths have rather minor effects. The ramp angles can have respectable influence on the compression efficiency, which is associated with the shock and viscous losses. The maximum pressure gradient can be highly sensitive to the ramp angles in conjunction with the ramp lengths, which determine the shock structures. A remarkable correlation has been found between the inlet drag and exit temperature, both of which are largely dependent on the combustor radius. Further investigation is needed to reveal the physical ground for this correlation as well as the decisive factors for the compression efficiency.

Acknowledgements

The authors are grateful to Dr. Tapabrata Ray and Amitay Isaacs at UNSW@ADFA for providing the advanced MDO capability developed in the group.

References

[1] Paull, A., Alesi, H. and Anderson, S., “HyShot Flight Program and How it was Developed”, AIAA Paper 2002-5248, Sep 2002.

[2] Boyce, R. R., Gerard, S. and Paull, A., “The HyShot Scramjet Flight Experiment – flight data and CFD calculations compared”, AIAA Paper 2003-7029, Dec 2003.

[3] McClinton, C. R., “X-43 – Scramjet Power Breaks the Hypersonic Barrier: Dryden Lectureship in Research for 2006”, AIAA Paper 2006-1-317, Jan 2006.

[4] Boeing, “X-51A WaveRider Breaks Record in 1st Flight”, http://boeing.mediaroom.com, May 2010.

[5] Hunt, D. C., Paull, A., Boyce, R. R. and Hagenmaier, M., “Investigation of an axisymmetric scramjet configuration utilising inlet-injection and radical farming”, *in Proceedings of the 19th International Symposium on Airbreathing Engines (ISABE 2009)*, Montréal, Sep 2009.

[6] Odam, J., Paull, A., “Radical Farming in Scramjets”, *Notes on Numerical Fluid Mechanics and Multidisciplinary Design*, Vol.96 (*eds.* Tropea, C., Jakirlic, S., Heinemann, H. J., Hinlinger, H.), Springer, Berlin, 2007.

[7] McGuire, J. R., Boyce, R. R. and Mudford, N. R., “Radical farm ignition processes in two-dimensional supersonic combustion”, *Journal of Propulsion and Power*, Vol. 24, No. 6, 2008, pp. 1248-1257.

[8] Ogawa, H., Grainger, A. L. and Boyce, R. R., “Numerical Investigation of Viscous Effects on Scramjet Inlet Starting”, *in Proceedings of 2009 Asia-Pacific International Symposium on Aerospace Technology*, Gifu, Japan, Nov 2009.

[9] Ogawa, H., Grainger, A. L. and Boyce, R. R., “Inlet Starting of High-Contraction Axisymmetric Scramjets”, *Journal of Propulsion and Power*, *in press*, 2010.

[10] Matthews, A. J., “Scramjet Intakes”, PhD Thesis, The University of Oxford, 2003.

[11] Ray, T. and Smith, W., “A Surrogate Assisted Parallel Multiobjective Evolutionary Algorithm for Robust Engineering Design”, *Engineering Optimization*, Vol. 38, No. 8, pp. 997-1011, 2006.

[12] Ray, T., Isaacs, A. and Smith, W., “Multi-

objective optimization using surrogate assisted evolutionary algorithm", (*Introduction G.P.Rangaiah*), *Multi-objective Optimization: Techniques and Applications in Chemical Engineering*, pp. 131-151, World Scientific, Singapore, 2008.

[13] Ogawa, H., Alazet, Y., Boyce, R. R., Isaacs, A. and Ray, T., "Design Optimisation of Axisymmetric Scramjets for Access-to-Space", *in Proceedings of the 9th Australian Space Science Conference 2009*, Sydney, Sep 2009.

[14] Ogawa, H., Boyce, R. R., Isaacs, A. and Ray, T., "Multi-Objective Design Optimisation of Inlet and Combustor for Axisymmetric Scramjets", *The Open Thermodynamics Journal*, *in press*, 2010.

[15] Billig, F. S. and Van Wie, D. M., "Efficiency Parameters for Inlets Operating at Hypersonic Speeds", ISABE 87-7047, 8th International Symposium on Airbreathing Engines, Cincinnati, USA, 1987.

[16] Van Wie, D. M., "Scramjet Inlets", *Scramjet Propulsion*, Progress in Astronautics and Aeronautics, Vol. 189, Eds. Curran, E. T. and Murthy, S. N. B., 2000.

[17] Paull, A. and Stalker, A. J., "Scramjet Testing in the T3 and T4 Hypersonic Impulse Facilities", *Scramjet Propulsion*, Progress in Astronautics and Aeronautics, Vol. 189, Eds. Curran, E. T. and Murthy, S. N. B., 2000.

[18] Mölder, S. and McGregor, R. J., "Analysis and Optimization of Scramjet Inlet Performance", ICAS Paper 90-4.7.3, 17th Congress of the Aeronautical Sciences, Stockholm, Sweden, Sep 1990.

[19] CFD++, Software Package, Ver. 8.11, Metacomp Technologies, Inc., CA, 2009.

[20] Bardina, J. E., Huang, P. G. and Coakley, T. J., "Turbulence Modeling Validation, Testing, and Development", NASA Technical Memorandum 110446, 1997.

[21] Pointwise, *Software Package*, Ver.16.02, Pointwise,Inc., TX, 2008.

[22] Deb, K., Pratap, A., Agarwal, S. and Meyarivan, T., "A fast and elitist multiobjective genetic algorithm: NSGA-II", *IEEE Transactions on Evolutionary Computation*, Vol. 6, No. 2, pp. 182-197, 2002.

[23] Saltelli, A., Ratto, M., Andres, T., Compolongo, F., Cariboni, J., Gatelli, D., Saisana, M. and Tarantola, S., *Global Sensitivity Analysis. The Primer*, Wiley, England, 2008.

[24] Sobol, I. M., "Uniformly distributed sequences with additional uniformity properties", *USSR Computational Mathematics and Mathematical Physics*, Vol.16, No.5, pp. 236-242, 1976.

[25] Quelpo, N. V., Haftka, R. T., Shyy, W., Goel, T., Vaidyanathan, R. and Tucker, K., "Surrogate-Based Analysis and Optimization", Progress in Aerospace Sciences, Vol. 41, No. 1, pp. 1-28, 2005.

Copyright Statement